Supporting Information for "The 2 May 2025 Mw 7.4 Drake Passage Earthquake: Insights into Tectonics at the Shackleton Fracture Zone–Chilean Trench Transition"

A. Vuan[1], G. Brancatelli[1], G. Brancolini[1], L. Gasperini[2], R. Geletti[1], E. Lodolo[1], A. Magrin[1], M. Menichetti[3], M. Plasencia[1], A. Polonia[2], M. Santulin[1], A. Tassone[4]

[1]Istituto Nazionale di Oceanografia e di Geofisica Sperimentale – OGS, Italy
[2]Istituto di Scienze Marine – CNR-ISMAR, Bologna, Italy
[3]Dipartimento di Scienze Pure ed Applicate, Università di Urbino, Urbino, Italy
[4]Instituto de Geociencias Básicas, Aplicadas y Ambientales de Buenos Aires (IGeBA), CONICET – Universidad de Buenos Aires, Argentina

Contents of this file

1. Text S1 to S5
2. Tables S1 to S6
3. Figures S1 to S9

S1 Relocation of the seismic events

The events of the 2 May 2025 seismic sequence were initially detected and located using our server, which monitors the area covered by the Antarctic Seismographic Argentinean Italian Network (ASAIN) in and around the Scotia Sea and the Antarctic Peninsula. In addition to data from our network, the SeisComP server (Helmholtz-Centre Potsdam–GFZ and Gempa, 2008) was configured to continuously receive data from approximately other 60 stations selected to detect events in the region (Table S1). Data from global networks were collected via international agencies and standard protocols. Between 2 May and 7 July 2025, the automatic monitoring system located 49 events following the Mw 7.4 mainshock in the Drake Passage, with magnitudes ranging between 4.0 and 6.4.

We manually reviewed the locations of the main events using only stations at regional distances ($< 28°$). We also relocated an additional event from March 27, 2007 (M 4.8), whose epicenter lies close to the 2025 sequence. The list of stations used in the relocation process is provided in Table S2, and Figure S1 shows their distribution together with the location of the mainshock. The two stations closest to the 2 May 2025 event are C1.MG01 (207 km) and AI.DSPA (316 km), both located in Tierra del Fuego. Other stations in southernmost South America lie up to ∼600 km away.

To achieve acceptable azimuthal coverage (azimuthal gap $< 180°$), we also included stations on the Antarctic Peninsula, in the Scotia Sea region, and in the nearest part of the polar plateau. Stations on the Antarctic Peninsula record fewer clear P phases than those in the polar region (with the exception of IU.PMSA), owing to high ambient noise levels (e.g., Vuan et al. (2000)). We selected P phases—and, for the closest stations, also S phases—and relocated the events using the LocSAT algorithm (Bratt & Nagy, 1991) together with the IASPEI91 velocity model (Kennett & Engdahl, 1991). When possible, event depths were left unfixed.

S2 Depth from pP and sP phases through machine learning models

The determination of earthquake depth using pP and sP phases involves analyzing the time difference between the arrival of these surface-reflected phases and the direct P wave. SeisBench, a framework for machine learning in seismology (Woollam et

al., 2022), facilitates this task by providing tools for robust identification of depth phases. The SeisBench interfaces *DepthPhaseTEAM* and *DepthPhaseNet* (Münchmeyer et al., 2023) allow users to input preliminary earthquake locations together with waveform data to estimate depth from the predicted arrival times of the pP and sP phases. DepthPhaseTEAM employs a multi-station probabilistic approach to determine event depth and quantify the associated uncertainties.

The workflow can be summarized as follows: (a) select high-quality stations at teleseismic distances; (b) predict approximate P-wave arrival times using global traveltime models; (c) download waveform data around these preliminary arrivals; (d) refine the P-wave picks using deep-learning–based predictions; and (e) estimate event depth using the IASPEI91 global velocity model and the time difference between the pP, sP, and direct P phases. This method is global in scope and does not account for potential biases in depth estimation caused by (1) local bathymetry or topography, (2) waveguides within the subducting plate that may introduce azimuthal variations, or (3) local shallow velocity structure (Münchmeyer et al., 2023).

The seismic data used in this analysis are freely available from the FDSN (Federation of Digital Seismological Networks; `https://www.fdsn.org/`), while preliminary earthquake locations were obtained from the GEOFON web services (`https://geofon.gfz.de/`). We used all available seismic stations located between 15° and 80° epicentral distance to evaluate potential pP and sP phases (Fig. S2). An initial station selection was performed by assessing the signal-to-noise ratio of the P-wave arrivals.

Hypocentral depth estimates are improved by incorporating teleseismic depth phases such as pP and sP, although identifying these phases remains challenging due to high ambient noise levels in the region. The robustness of pP–P-derived depth estimates is evaluated in Fig. S6, where observed delay times (Δt) are compared with parametric sensitivity curves describing the dependence of inferred depth on (a) the assumed crustal P-wave velocity V_p, (b) the P-wave takeoff angle θ, and (c) the thickness L of a shallow low-velocity layer (LVL).

S3 Multichannel seismic reflection data and focal solutions

Multichannel seismic reflection profile IT97–245 was acquired off Tierra del Fuego by the Italian R/V *OGS-Explora* during the 1997 expedition, as part of the Italian Antarctic Research Program (Polonia et al., 2007). The multichannel seismic data were recorded using a 3000 m long SERCEL-357 streamer with 120 active channels and a 50 m shot interval, providing a nominal fold of 30 and a sampling interval of 2 ms. The source consisted of a 36-gun array with a total volume of 80 L.

A broadband processing sequence was applied at the OGS computing center to improve the signal-to-noise ratio by attenuating both coherent and incoherent noise (Fig. S3). The processing workflow included denoising, deghosting, multiple attenuation, amplitude recovery and balancing, multichannel predictive deconvolution, iterative velocity analysis, pre-stack time migration, and final post-stack time-variant filtering (Brancatelli et al., 2022).

Focal solutions discussed later in the text are retrieved from the Global CMT catalog (Dziewonski et al., 1981; Ekström et al., 2012) and compared with focal mechanisms determined from regional data and other agencies. Given the scarcity of nearby seismic stations, we rely primarily on globally available sources for focal mechanism information, including the Global Centroid Moment Tensor (GCMT) catalog from Harvard, USGS, Geoscience Australia, and GFZ (Table S3). These agencies use different global datasets and apply different inversion procedures. The principal differences between the Harvard/GCMT and the USGS solutions for large earthquakes (Mw $>$ 7) arise from their inversion methodologies: the GCMT approach relies on centroid moment tensor inversion using long-period

surface waves and body waves, resolving the centroid location, which may differ significantly from the hypocenter; whereas the USGS typically employs a W-phase inversion for rapid, robust solutions, and may later provide additional products such as finite-fault models or multiple moment-tensor solutions (e.g., GCMT-style inversions or full-waveform approaches). Despite these methodological differences, both the GCMT and USGS place the 2025 mainshock at depths of 20 km or greater, which likely explains why no significant tsunami amplitudes were recorded.

S4 Tables

The following tables summarize the seismic and station datasets used in this study. Table S1 lists all seismic stations configured in the SeisComP monitoring system for automatic detection and location of regional earthquakes. Table S2 provides detailed station parameters and statistics of P- and S-phase arrivals used in the relocation procedure. Table S3 reports the focal mechanism solutions for the May 2, 2025 mainshock obtained from global agencies. Table S4 compiles GCMT fault-plane solutions since 1976 in the study area, highlighting the predominance of steeply dipping mechanisms. Table S5 includes GCMT mechanisms for earlier aftershocks of the 2025 sequence while Table S6 shows the catalog of relocated earthquakes. Together, these tables document the observational foundation for the seismic analysis presented in the main text.

Table S1. Stations used by SeisComp server for automatic detection and location.

Network	**Stations**
AI	BELA, DSPA, JUBA, MBIO, ORCD, PTRA, SMAI
AU	MAW
AW	VNA1, VNA2, VNA3
C	GO04, GO06, GO08, GO10
C1	AC04, AY02, AY03, AY04, AY05, BI02, BO04, CO01, CO02, IN44, LL01, LL02, LL03, LL04, LL05, LL06, LR05, MG01, MG02, MG03, MG04, MG05, MT09
G	CCD, COYC, DRV, TRIS
GE	SNAA
GT	BOSA, CPUP, LBTB, LPAZ, PLCA, VNDA
II	EFI, HOPE, RPN
IU	LCO, PMSA, QSPA

S5 Figures

The following figures illustrate the datasets, analytical steps, and structural interpretations supporting the results presented in this study. Figure S1 shows the distribution of stations used for manual revision of the seismic sequence, while Figure S2 displays the hypocentral location of the May 2, 2025 mainshock together with the stations employed for depth-phase evaluation. Figure S3 presents the uninterpreted multichannel seismic profile IT97–245, and Figure S4 summarizes station residuals used during event relocation. Figure S5 illustrates epicentral uncertainty ellipses for the revised events. Figure S6 provides the sensitivity analysis of depth estimates based on pP–P delays, and

Table S2. Station parameters used in the SeisComp relocation procedure.

net	sta	lon	lat	neve	np	ns	res_p	rms_p	D (deg)	azim
AI	BELA	-34.63	-77.88	9	9	0	-0.0	0.4	23.6	163.3
AI	DSPA	-68.27	-53.95	20	11	9	-0.0	1.3	3.2	352.8
AI	JUBA	-58.66	-62.24	2	2	0	-0.8	1.2	6.9	142.2
AI	MBIO	-56.62	-64.24	2	2	0	-0.1	1.0	9.2	147.9
AI	ORCD	-44.74	-60.74	3	3	0	-0.1	0.6	12.4	117.0
AI	PTRA	-56.23	-63.48	1	1	0	0.2	0.0	8.5	142.3
AI	SMAI	-67.11	-68.13	3	3	0	0.3	0.7	11.1	179.2
AW	VNA1	-8.28	-70.69	3	3	0	0.1	0.4	27.8	142.3
AW	VNA2	-7.39	-70.92	6	6	0	-0.4	0.4	28.1	142.9
AW	VNA3	-9.67	-71.24	6	6	0	-0.3	0.4	27.4	143.5
C	GO06	-71.47	-39.58	5	5	0	1.0	0.5	17.8	350.4
C	GO08	-72.56	-48.46	7	7	0	1.2	1.9	9.2	339.1
C	GO10	-71.05	-53.15	7	7	0	-0.5	0.9	4.5	331.5
C1	AC04	-71.07	-28.20	6	6	0	-0.4	0.4	29.1	353.6
C1	AY02	-73.19	-46.48	2	2	0	1.7	0.6	11.1	339.4
C1	AY03	-72.59	-47.25	4	4	0	1.4	0.4	10.4	340.4
C1	AY04	-71.69	-46.58	1	1	0	1.1	0.0	11.1	343.5
C1	AY05	-73.51	-45.15	5	5	0	0.6	1.6	12.6	340.1
C1	BI02	-71.27	-36.66	8	8	0	0.2	0.6	20.7	351.6
C1	BO04	-70.61	-33.99	1	1	0	-0.4	0.0	23.1	353.6
C1	CO01	-70.09	-29.98	8	8	0	0.5	0.5	27.3	355.3
C1	CO02	-71.00	-31.20	7	7	0	-0.2	0.5	26.1	353.2
C1	IN44	-59.66	-62.48	2	2	0	-0.3	0.7	6.8	147.2
C1	LL01	-72.41	-42.38	5	5	0	1.9	1.7	15.2	345.9
C1	LL02	-71.85	-43.19	8	8	0	1.5	1.7	14.2	347.5
C1	LL03	-72.40	-41.14	4	4	0	0.6	0.2	16.4	346.5
C1	LL04	-72.41	-40.91	4	4	0	0.7	0.2	16.6	346.8
C1	LL05	-73.47	-41.41	6	6	0	1.3	0.9	16.2	343.7
C1	LR05	-72.00	-40.23	7	7	0	1.1	0.7	17.2	348.4
C1	MG01	-67.63	-54.93	19	11	8	-1.6	0.7	2.2	359.9
C1	MG02	-69.22	-52.78	12	10	2	-0.9	0.6	4.5	347.4
C1	MG03	-70.46	-53.85	18	10	8	-1.0	0.6	3.7	332.7
C1	MG04	-71.57	-52.86	11	8	3	-1.5	0.8	4.8	330.7
C1	MG05	-72.50	-51.68	1	1	0	-2.9	0.0	5.8	334.7
C1	MT09	-70.99	-33.78	7	7	0	-1.0	0.2	23.6	352.7
GE	SNAA	-2.84	-71.67	7	7	0	-0.7	0.6	29.7	144.6
GT	CPUP	-57.33	-26.33	2	2	0	-2.1	0.6	31.7	17.4
GT	LPAZ	-68.13	-16.29	3	3	0	0.1	0.5	40.7	358.8
GT	PLCA	-70.55	-40.73	9	9	0	1.3	1.5	16.6	352.0
GT	VNDA	161.85	-77.52	1	1	0	1.0	0.0	42.3	194.2
II	EFI	-58.06	-51.68	2	1	1	-0.3	0.0	7.5	47.8
II	HOPE	-36.49	-54.28	8	8	0	0.7	0.3	17.6	93.7
IU	LCO	-70.70	-29.01	6	6	0	-0.1	0.6	28.3	354.1
IU	PMSA	-64.05	-64.77	11	11	0	-0.0	0.6	7.9	169.0
IU	QSPA	144.44	-89.93	1	1	0	1.0	0.0	33.2	180.1
IU	TRQA	-61.98	-38.06	1	1	0	0.1	0.0	19.3	12.1

Table S3. Focal solutions available for the mainshock – GCMT = Global Centroid Moment Tensor Harvard, USGS = United States Geological Survey, GAUS = Geoscience Australia, GFZ = Helmholtz Centre for Geosciences.

Agency	Strike1	Dip1	Rake1	Strike2	Dip2	Rake2	Mw	Depth (km)
GCMT	326	38	99	134	52	83	**7.4**	**20**
USGS	310	33	93	128	57	88	**7.4**	**23.5**
GAUS	348	45	134	115	59	56	**7.5**	**12**
GFZ	152	60	93	326	30	84	**7.45**	**10**

Table S4. Fault plane solutions from GCMT since 1976 in the area. Close to the mainshock of May 2, 2025, the dip angles are greater than 34°. Some mechanisms at higher dip are strike slip events.

Lon	Lat	Strike	Dip	Rake	Strike1	Dip1	Rake1	Man	Exp	Datetime
-66.69	-57.42	300	41	57	160	57	115	1.350	24	1980050200
-65.02	-58.30	294	66	-8	27	83	-156	1.410	24	1984040500
-66.90	-57.56	167	90	180	257	90	0	1.690	24	1987062100
-66.38	-57.22	189	79	169	281	79	11	6.500	23	1991060300
-66.42	-57.67	115	45	56	339	54	119	7.690	24	1995030100
-66.16	-57.94	112	70	16	16	75	159	2.887	25	2010011712
-66.33	-57.75	334	44	97	144	46	83	5.593	23	2010012019
-65.76	-57.59	201	82	179	291	89	8	2.833	25	2012041410
-66.85	-57.74	130	49	-1	220	89	-139	5.132	23	2015031400
-65.99	-57.48	208	79	-169	115	79	-12	2.376	24	2015102020
-66.75	-57.42	341	38	99	149	53	83	3.436	23	2016031003
-68.98	-56.78	27	72	167	121	78	19	2.805	23	2016071121
-69.11	-56.74	34	74	173	126	83	17	3.191	23	2016071121
-66.60	-57.55	140	42	67	349	52	109	3.874	25	2018102906
-66.43	-57.69	121	46	48	353	58	125	6.678	24	2018102920
-66.55	-57.66	130	38	48	359	63	118	3.461	24	2018102921
-66.49	-57.40	171	38	107	329	54	77	3.872	23	2018103112
-66.22	-57.48	334	46	75	176	46	105	3.409	23	2018110816
-66.41	-57.59	170	43	112	321	51	71	6.495	23	2018111607
-66.32	-57.79	108	54	35	355	63	138	8.307	23	2019090516
-67.79	-57.17	323	34	85	149	57	93	3.702	23	2019122120

Table S5. GCMT focal mechanisms for earlier aftershocks of the May 2, 2025, event.

Lon	Lat	Strike	Dip	Rake	Strike1	Dip1	Rake1	Mantissa	Exp	Datetime
-67.22	-57.38	326	37	105	128	55	79	4.264	25	2025050217
-67.21	-57.15	23	61	176	115	86	29	6.715	23	2025052100
-67.06	-57.43	304	43	74	145	49	104	1.059	24	2025060711
-67.24	-57.18	22	72	-170	289	81	-18	3.009	24	2025070415

Figure S7 represents the depth-phase likelihood per-event. Figure S8 shows rose diagrams of P- and T-axis azimuths derived from focal mechanisms. Finally, Figure S9 depicts the temporal and spatial variation of dip angles within the study area. Together, these fig-

Table S6. Relocated earthquake catalog for the 2 May 2025 seismic sequence. Events with fixed depths of 10 km represent poorly constrained hypocentral depths and are not considered in the figures.

Datetime	**Lon**	**Lat**	**Depth (km)**	**Magnitude**
Datetime (UTC)	Longitude	Latitude	Depth (km)	Magnitude
2025-05-02T12:58:30.714600Z	-67.9629	-56.7823	24	7.35
2025-05-02T13:07:50.723674Z	-68.4773	-56.8318	37	6.30
2025-05-02T13:09:45.025968Z	-67.3407	-57.3206	38	6.21
2025-05-02T13:49:32.046682Z	-67.1248	-57.2899	10	5.56
2025-05-02T13:55:07.375365Z	-67.8175	-57.2570	38	5.82
2025-05-02T14:12:30.267208Z	-67.4643	-57.0602	10	5.07
2025-05-02T14:38:09.028517Z	-67.4721	-57.0434	27	5.52
2025-05-02T14:43:50.413312Z	-67.5991	-57.3460	37	5.05
2025-05-02T15:18:10.330631Z	-67.5879	-56.8436	38	4.75
2025-05-02T15:25:40.448081Z	-66.5682	-57.3580	10	5.08
2025-05-02T15:42:56.100781Z	-67.3891	-57.2158	29	4.93
2025-05-02T15:59:12.220271Z	-67.4493	-56.6517	10	4.38
2025-05-02T16:13:07.028555Z	-66.3910	-56.9893	10	4.72
2025-05-02T16:48:36.823690Z	-67.7325	-57.4281	29	5.43
2025-05-02T16:48:37.093707Z	-67.5468	-57.4320	28	5.41
2025-05-02T17:59:12.913532Z	-67.1428	-57.2977	28	6.39
2025-05-02T18:20:33.972119Z	-68.1114	-57.6818	36	5.10
2025-05-02T19:33:53.546626Z	-67.0771	-57.3481	32	5.26
2025-05-02T19:42:33.644644Z	-67.8049	-57.0214	10	4.88
2025-05-02T19:58:04.140328Z	-66.8737	-57.3816	53	4.81
2025-05-02T20:14:17.834638Z	-67.4167	-57.1532	24	5.54
2025-05-02T22:07:18.493313Z	-66.0444	-55.1214	10	4.02
2025-05-03T10:06:33.411526Z	-67.6346	-57.0769	8	5.30
2025-05-03T10:50:47.790306Z	-67.3134	-57.2732	39	4.91
2025-05-04T04:38:09.589914Z	-67.7725	-57.6115	26	5.33
2025-05-04T23:24:25.260051Z	-68.0753	-56.8818	0	4.95
2025-05-07T18:47:19.990652Z	-67.6708	-57.0634	10	4.36
2025-05-08T00:36:17.150634Z	-67.1085	-57.1416	12	4.88
2025-05-24T05:32:14.667002Z	-68.5359	-56.9413	0	5.40
2025-06-07T11:06:09.491138Z	-67.1834	-57.3681	41	5.44

126 ures document the seismological and structural constraints underpinning the interpre-
127 tation of the 2025 seismic sequence.

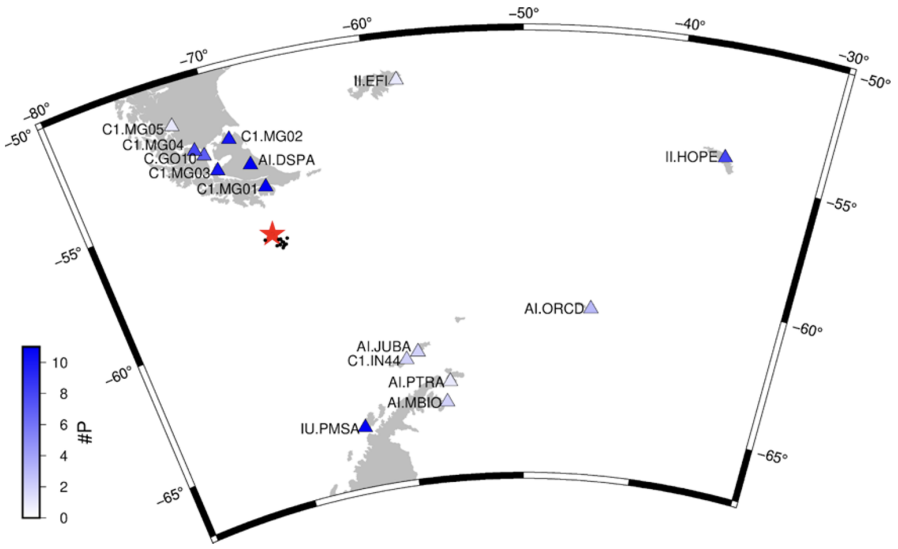


Figure S1. Stations used for manual revision; the color indicates the number of P-phases used for each station.

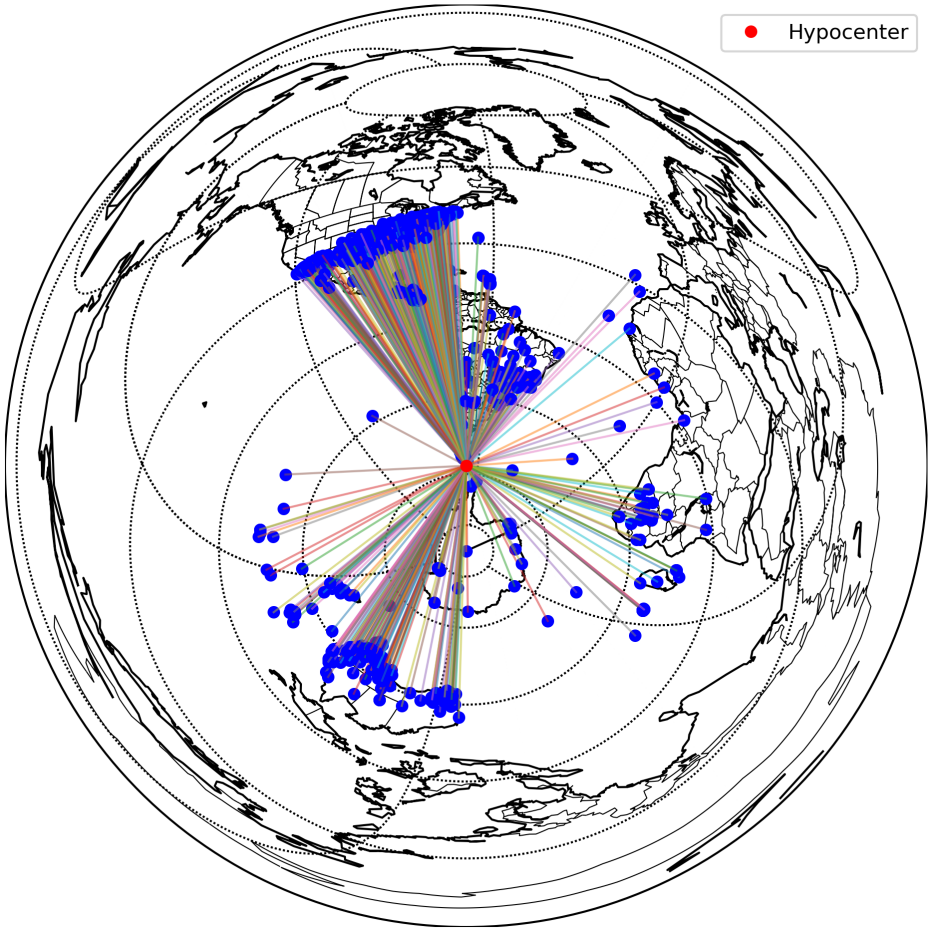


Figure S2. Figure S2. Hypocenter location of the 2 May 2025 mainshock and seismic stations (blue dots) used to constrain depth from pP–P differential times. Waveform data were retrieved from the GEOFON data center. Stations are at epicentral distances from 15° to 80°.

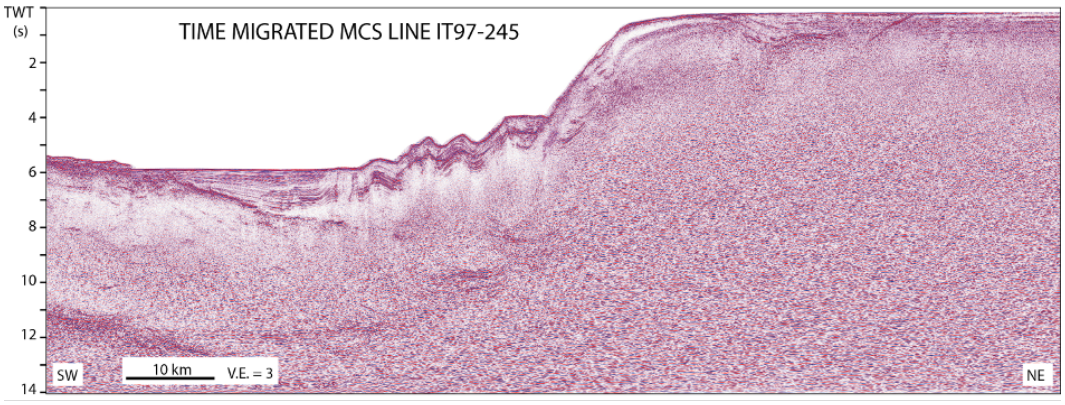


Figure S3. Uninterpreted multichannel seismic line IT97-245 described in this work.

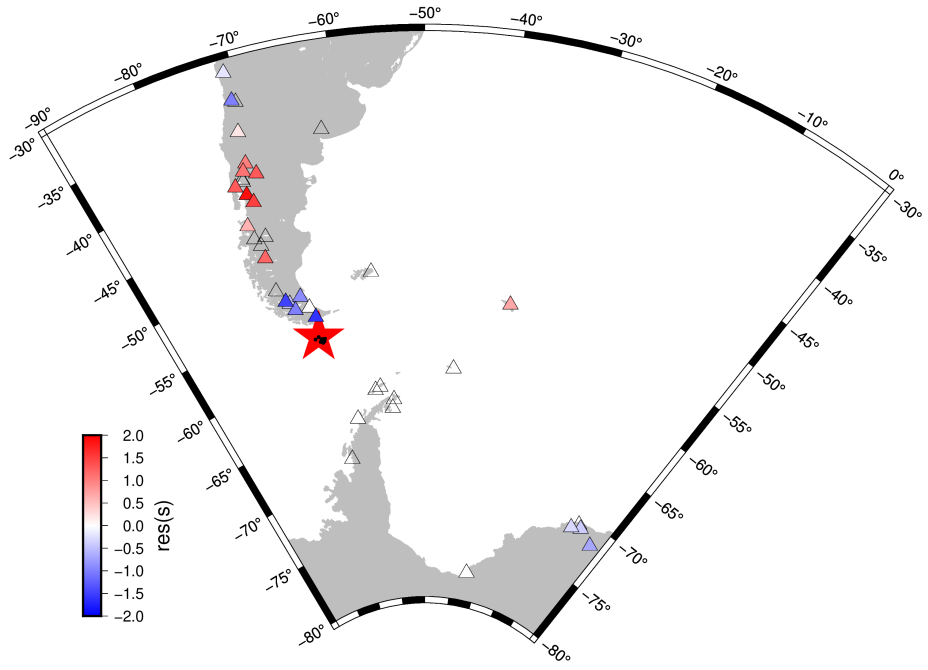


Figure S4. Stations used for the relocation of events. The color scale shows the average residual for each station when more than 5 P-phases are available.

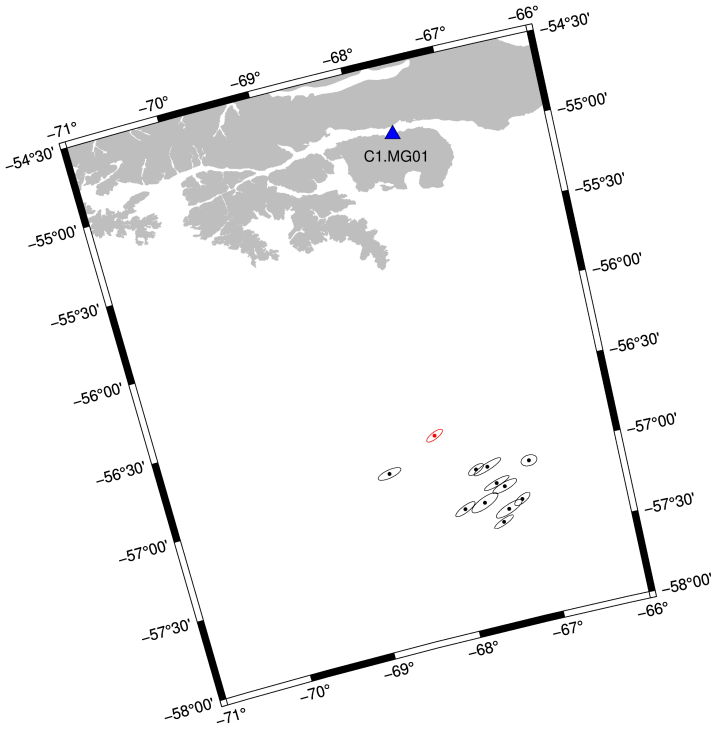


Figure S5. Uncertainty ellipses of the epicenters for the revised events. Location of the mainshock and uncertainty ellipse in red.

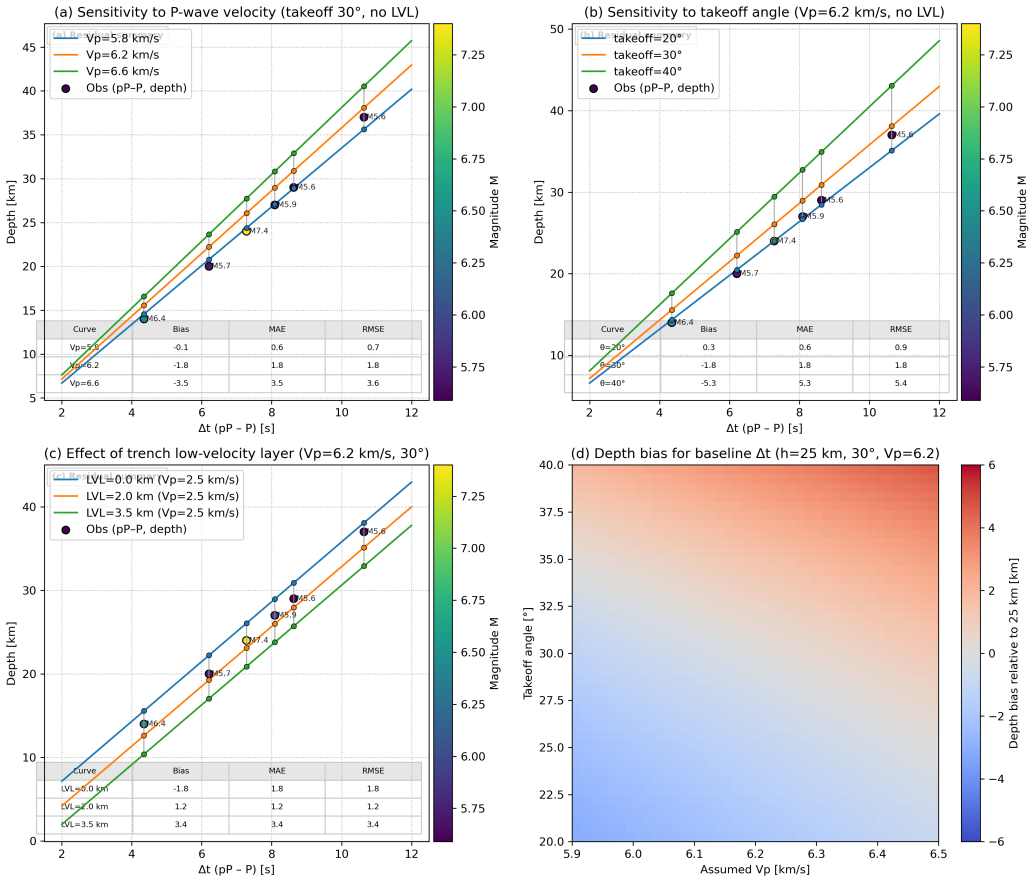


Figure S6. Sensitivity of pP–P–inferred depths with panel-wise residuals. (a) Depth inferred from the pP–P delay Δt for different crustal P-wave velocities V_p (takeoff angle 30°; no low-velocity layer, LVL). (b) Depth versus Δt for different takeoff angles θ ($V_p = 6.2$ km/s; no LVL). (c) Depth versus Δt for different LVL thicknesses. Observed events are plotted as circles at (Δt, estimated depth). For each observation, a thin vertical line at the measured Δt carries colored markers indicating the depths predicted by each sensitivity curve in the panel. The on-panel summary tables report the bias, mean absolute error (MAE), and root mean square error (RMSE), all in km, of the residuals defined as $\text{Depth}_{\text{obs}} - \text{Depth}_{\text{inf}}(\Delta t;$ panel parameters), where positive residuals imply underestimation by the model. (d) Heat map of depth bias (for an inferred depth of 25 km) as a function of assumed V_p and θ.

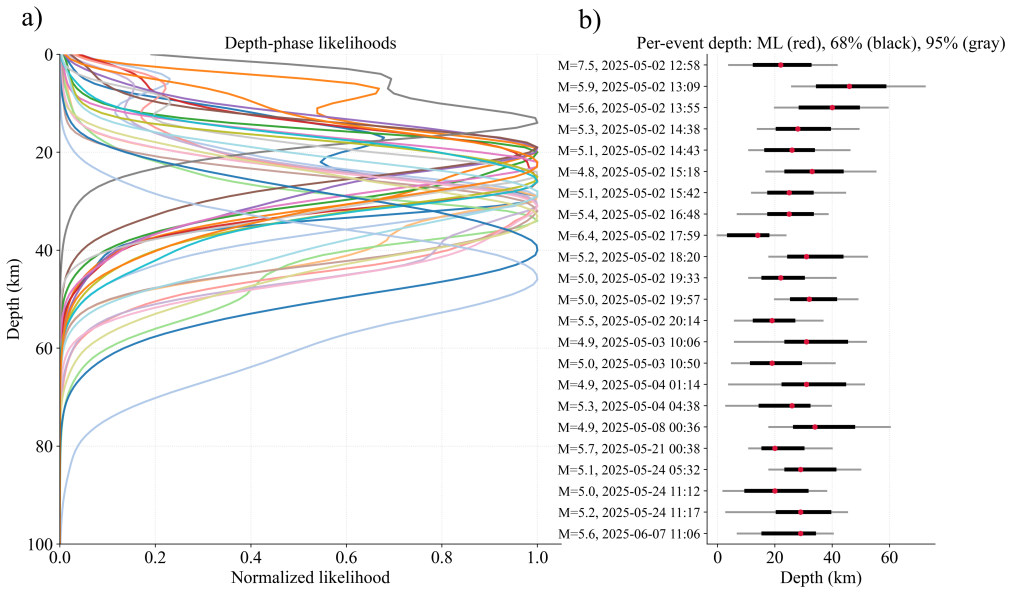


Figure S7. a) Normalized depth–phase likelihood functions for all analyzed events (left), computed from waveform-based depth-phase modeling using pP–P, sP–P, and related teleseismic depth-sensitive arrivals. For each event, the likelihood curve is shown with its 68% highest posterior density (HPD) credible region, obtained via marginalization over phase picks and modeling uncertainties. Shading indicates the depth intervals where the posterior probability exceeds the 68% HPD threshold. b) Per-event depth solutions, including the maximum-likelihood (ML) depth estimate (red marker), 68% posterior credible interval (black bars), and 95% credible interval (gray bars). Events are ordered by origin time, and their magnitudes and timestamps are annotated accordingly. The reviewed centroid depth of the Mw 7.4 mainshock reported by the USGS is consistent with our estimate.

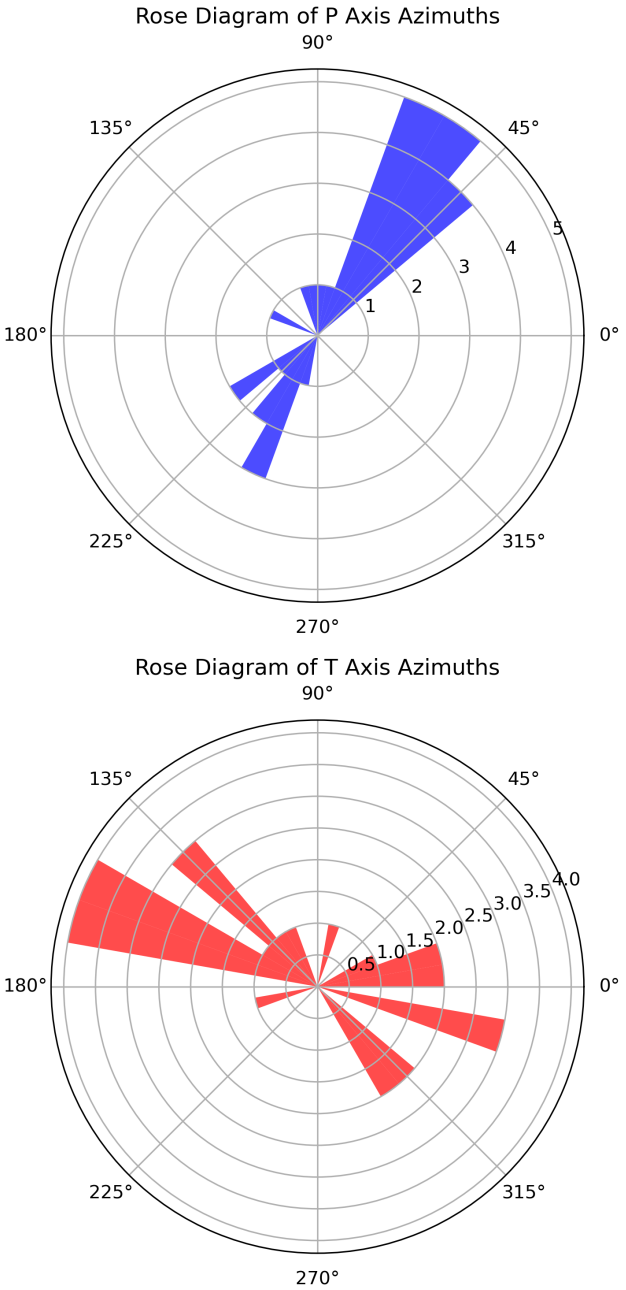


Figure S8. Rose diagrams showing the directional distribution of P- and T-axis azimuths derived from focal mechanism solutions. The top panel illustrates the frequency of P-axis orientations, while the bottom panel shows T-axis orientations. Each bar represents the number of events with azimuths falling within 10° directional bins, highlighting dominant stress orientations in the region.

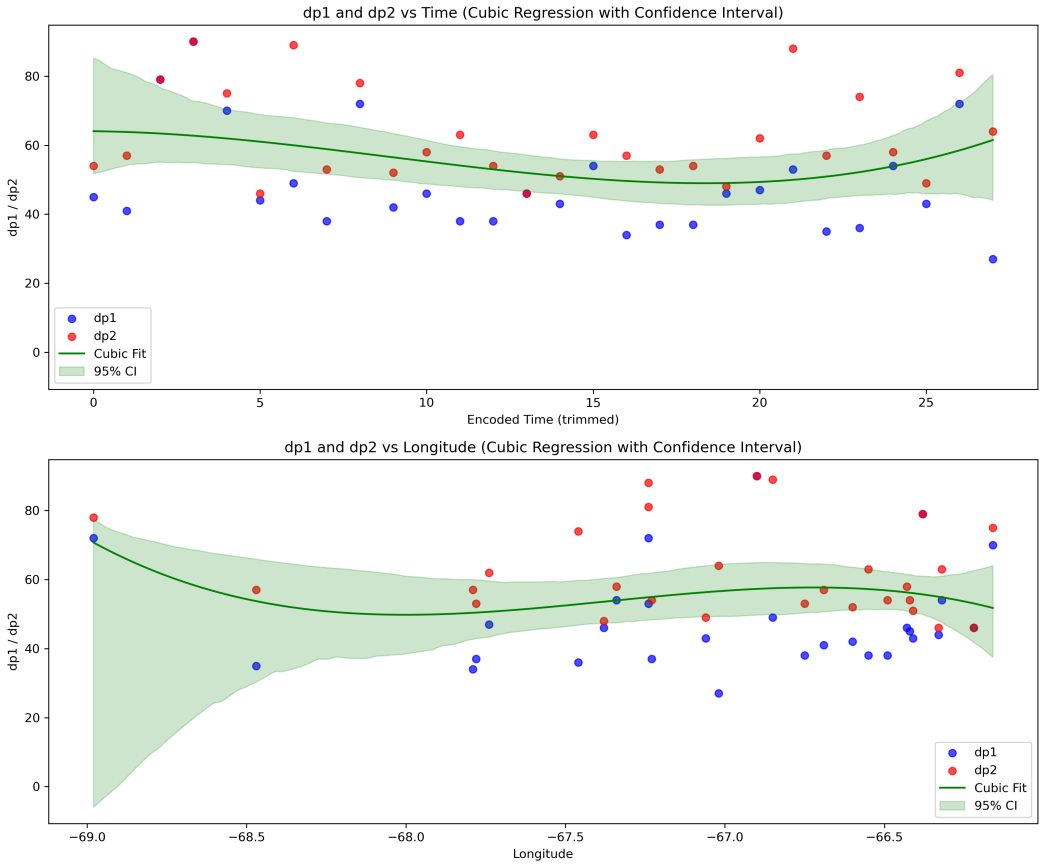


Figure S9. (top) Temporal and (bottom) spatial variation of dip angles from collected focal mechanisms in the study area. The plot illustrates changes in fault-plane dip angles as a function of event time and longitude, providing insights into the evolution of rupture geometry and deformation style during the seismic sequence. Variations in dip may reflect differences in fault orientation, stress regime, and structural segmentation along the plate boundary.

References

Brancatelli, G., Forlin, E., Bertone, N., Del Ben, A., & Geletti, R. (2022). Chapter 7 - time to depth seismic reprocessing of vintage data: A case study in the Otranto Channel (South Adriatic Sea). In R. Bell, D. Iacopini, & M. Vardy (Eds.), *Interpreting subsurface seismic data* (p. 157-197). Elsevier. doi: 10.1016/B978-0-12-818562-9.00009-1

Bratt, S. R., & Nagy, W. (1991). *The LocSAT Program* (Tech. Rep.). San Diego, CA: Science Applications International Corporation (SAIC). (User manual/report)

Dziewonski, A. M., Chou, T.-A., & Woodhouse, J. H. (1981). Determination of earthquake source parameters from waveform data for studies of global and regional seismicity. *Journal of Geophysical Research: Solid Earth*, *86*(B4), 2825–2852. doi: 10.1029/JB086iB04p02825

Ekström, G., Nettles, M., & Dziewonski, A. M. (2012). The global CMT project 2004–2010: Centroid-moment tensors for 13,017 earthquakes. *Physics of the Earth and Planetary Interiors*, *200–201*, 1–9. doi: 10.1016/j.pepi.2012.04.002

Kennett, B. L. N., & Engdahl, E. R. (1991). Traveltimes for global earthquake location and phase identification. *Geophysical Journal International*, *105*(2), 429–465. doi: 10.1111/j.1365-246X.1991.tb06724.x

Münchmeyer, J., Saul, J., & Tilmann, F. (2023). Learning the Deep and the Shallow: Deep-Learning-Based Depth Phase Picking and Earthquake Depth Estimation. *Seismological Research Letters*, *95*(3), 1543–1557. doi: 10.1785/0220230187

Polonia, A., Torelli, L., Brancolini, G., & Loreto, M.-F. (2007). Tectonic accretion versus erosion along the southern Chile trench: Oblique subduction and margin segmentation. *Tectonics*, *26*, TC3005. doi: 10.1029/2006TC001983

Vuan, A., Russi, M., & Panza, G. (2000). Group Velocity Tomography in the Subantarctic Scotia Sea Region. *Pure and Applied Geophysics*, *157*, 1337–1357. doi: 10.1007/PL00001122

Woollam, J., Münchmeyer, J., Tilmann, F., Rietbrock, A., Lange, D., Bornstein, T., ... Soto, H. (2022). SeisBench—A Toolbox for Machine Learning in Seismology. *Seismological Research Letters*, *93*(3), 1695–1709. doi: 10.1785/0220210324